Editors' Suggestion

Compact High-Resolution Absolute-Gravity Gradiometer Based on Atom Interferometers

Wei Lyu,[1,2] Jia-Qi Zhong,[1,*] Xiao-Wei Zhang,[1] Wu Liu,[1,2] Lei Zhu,[1] Wei-Hao Xu,[1,2] Xi Chen,[1] Biao Tang,[1] Jin Wang,[1,3,†] and Ming-Sheng Zhan[1,3,‡]

[1] *State Key Laboratory of Magnetic Resonance and Atomic and Molecular Physics, Innovation Academy for Precision Measurement Science and Technology, Chinese Academy of Sciences, Wuhan 430071, People's Republic of China*

[2] *School of Physical Sciences, University of Chinese Academy of Sciences, Beijing 100049, People's Republic of China*

[3] *Wuhan Institute of Quantum Technology, Wuhan 430206, People's Republic of China*

(Received 24 February 2022; revised 20 May 2022; accepted 19 October 2022; published 30 November 2022)

We present a compact high-resolution absolute-gravity gradiometer based on dual ^{85}Rb atom interferometers using stimulated Raman transitions. A baseline of $L = 44.5$ cm and an interrogation time of $T = 130$ ms are realized in a sensor head with a volume of only 95 l. Many experimental parameters are optimized to improve the short-term sensitivity, whereas interleaving measurements by reversing the direction of the Raman wave vector are implemented to improve the long-term stability. After an averaging time of 17 000 s, a phase resolution of 104 μrad is achieved, which corresponds to a gravity-gradient resolution of 0.86 E (1 E = $1 \times 10^{-9}/s^2$). After the evaluation and correction of systematic errors induced by light shift, the residual Zeeman shift, the Coriolis effect, the self-attraction effect, etc., the instrument serves as an absolute-gravity gradiometer and with it the local gravity gradient is measured to be 3114 (53) E. This instrument combines the merits of high-resolution, high-compactness and high-accuracy, and has good application prospects in many fields.

DOI: 10.1103/PhysRevApplied.18.054091

I. INTRODUCTION

Gravimetry technology plays a significant role in the fields of metrology, geology, geophysics, seismology, and industry-related applications such as resource exploration and autonomous navigation. Since its inception in 1991 [1], the light-pulse atom interferometer (LPAI) has attracted great interest in the field of gravity measurements and has demonstrated remarkable resolution and long-term stability [2–7]. After three decades of development, gravimeters based on LPAIs have achieved such high maturity that six LPAI gravimeters have taken part in the 10th International Comparison of Absolute Gravimeters (ICAG) in 2017 and shown performance that competes with the classic corner-cube gravimeters [8–10]. Marine and airborne LPAI gravimeters have also been developed and have shown performance beyond that of spring gravimeters [11,12].

In comparison with gravimeters, gravity gradiometers could map subsurface density variations with higher spatial resolution. Also, due to the differential measurement mode, gravity gradiometers are highly immune from acceleration noise, which makes them useful in situations where vibration noise hampers gravity measurements. In LPAI-based gravity gradiometers [13], simultaneous atom interferometers (AIs) are manipulated by a common series of Raman laser pulses, which brings about the additional advantage of common-mode rejection of many internal noises.

The absolute measurement accuracy and the compactness of the system are two important aspects of such an instrument. An absolute-gravity gradiometer could calibrate relative gradiometers and absolute gravimeters, as well as measure the vertical deflection during the moving process, which is of great significance in the field of navigation. Meanwhile, a compact gravity gradiometer can be integrated with an inertial stabilized platform and perform onboard gravity mapping over a wide area. However, in the literature, more works are focused on using the LPAI gravity gradiometers to measure the Newtonian gravitational constant [14–19], where people only pay heed to the relative changes of the gravity gradient produced by moving masses. Only a few research works have been reported about the evaluation of the absolute-gravity gradient [20] and there is still a lack of comprehensive investigation on

*jqzhong@apm.ac.cn
†wangjin@apm.ac.cn
‡mszhan@apm.ac.cn

the systematic errors of LPAI-based gravity gradiometers. With respect to compactness, the atom-gravity gradiometer in iXblue has recently reached an unprecedented resolution [21], and that in Birmingham has demonstrated outdoor application in tunnel detection [22]. However, the dimensions of their sensor heads, especially the heights (1.75 m and 1.87 m, respectively), still make it somewhat inconvenient to carry and to take onto forms of transportation for onboard measurement.

In this paper, we present a highly integrated solution for high-precision gravity-gradient measurement based on ^{85}Rb atom interferometers and demonstrate a comprehensive set of methods for evaluating and analyzing the systematic errors. To achieve a longer baseline, a higher data rate, and more interrogation time within a smaller sensor head, two fountain-type all-glass vacuum chambers with two-dimensional (2D) magneto-optical traps (MOTs) are fabricated. To improve the sensitivity, many parameters are optimized. In addition to reducing the measurement noise, investigations are also performed to reduce the cycle time. To improve the long-term stability, an algorithm relying on reversal of the Raman wave vector $\mathbf{k}$ is implemented and thus the k-polarity-independent drift is significantly removed. The improved short-term sensitivity and long-term stability lead to a measurement resolution as low as 0.86 E after an integration of 17 000 s. Finally, the measurement error for the absolute-gravity gradient is studied comprehensively. Besides those caused by Zeeman shifts, self-attraction, and the Coriolis effect, a special measurement error caused by the Raman laser scheme based on a chirping acousto-optical modulator (AOM) is also evaluated.

II. PRINCIPLE AND APPARATUS

Our gravity gradiometer is based on two vertically stacked atom interferometers (AIs) for the measurement of the differential acceleration. In each AI, the cold-atom cloud is split, redirected, and recombined by three Raman laser pulses, which are analogous to the beam splitter and mirrors in optical Mach-Zehnder interferometers. Since the excited atoms are imprinted by the phase of the Raman laser pulses, the phase shift of AI induced by gravity $\mathbf{g}$ can be written as

$$\Delta\phi = \phi_1 - 2\phi_2 + \phi_3 = \mathbf{k}_{\text{eff}} \cdot \mathbf{g}T^2, \tag{1}$$

where $\phi_i = \mathbf{k}_{\text{eff}} \cdot \mathbf{z}_i$, $(i = 1, 2, 3)$ are the laser phases and T is the interrogation time between the Raman pulses.

For two AIs A and B separated by $\mathbf{L}$, the phase difference caused by the gravity gradient is

$$\Delta\varphi_{\text{diff}} = \Delta\varphi_A - \Delta\varphi_B = \mathbf{k}_{\text{eff}} \cdot \Delta\mathbf{g}T^2. \tag{2}$$

The gravity gradient can then be calculated by

$$\Gamma = \Delta\varphi_{\text{diff}}/(\mathbf{k}_{\text{eff}} \cdot \mathbf{L}T^2). \tag{3}$$

In most cases, for gravity-gradient measurement, we only care about the acceleration difference rather than the exact accelerations at either position of the two gravimeters. Therefore, we usually use the least-squares fitting of the two interferometer signal P_A and P_B with the ellipse algebraic formula [23]

$$aP_A^2 + bP_AP_B + cP_B^2 + dP_A + eP_B + f = 0 \tag{4}$$

to evaluate the parameters (a, b, c, d, e, f) and obtain the differential phase

$$\Delta\varphi_{\text{diff}} = \cos^{-1}(-b/(2\sqrt{ac})). \tag{5}$$

In our experiment, ^{85}Rb atoms are laterally precooled by 2D MOTs and transferred to 3D MOTs for further cooling and trapping. With the loading time of 100 ms $\sim$ 2 s, about $1.2 \sim 9.0 \times 10^8$ atoms are able to be trapped. Then, cold-atom clouds with a temperature of about 2.8 μK are launched upward at a velocity of about 1.8 m/s by moving optical molasses. During the flight, the atoms are first prepared into a magnetically insensitive state with a magnetic quantum number $m_F = 0$. Then, a Raman laser pulse sequence $\pi/2$-π-$\pi/2$ is applied. The first and the third pulses have a duration of $\tau_1 = \tau_3 = \pi/(2\Omega) = 4$ μs and that of the second pulse has a duration of $\tau_2 = \pi/\Omega = 8$ μs, where Ω is the two-photon Rabi frequency. During the interaction with the photons, the excited atoms acquire recoil momentum, which makes the wave packet split and then become redirected and recombined. At the end of a measurement cycle, the populations in both ground states are detected successively and the ellipse fitting of the normalized populations,

$$P_A^{\text{nom}} = {P_A}^{F=3}/({P_A}^{F=3} + \eta_A {P_A}^{F=2}), \tag{6a}$$

$$P_B^{\text{nom}} = {P_B}^{F=3}/({P_B}^{F=3} + \eta_B {P_B}^{F=2}), \tag{6b}$$

is finally performed. η_A and η_B are the relative detection efficiencies for the states $|F = 3\rangle$ and $|F = 2\rangle$ in the two AIs, respectively. In our gradiometer, the two AIs have their own detection systems, which leads to a small difference of about 5% between the efficiencies. With this normalized detection, the signal-to-noise ratio is improved from 200:1 to about 400:1.

The design and a photograph of the sensor head are shown in Fig. 1. To reduce the preparation time of the two atom fountains and achieve a higher data rate, two identical atom-fountain setups are employed. Each of them has its own 2D and 3D MOT, which enable the two cold-atom clouds and fountains to be prepared simultaneously. Compared to the juggling scheme [16,17], where the two clouds come from the same 3D MOT, this scheme allows us to realize a relatively higher sampling rate up to 1.70 Hz (about 600 ms for each measurement) at the expense of

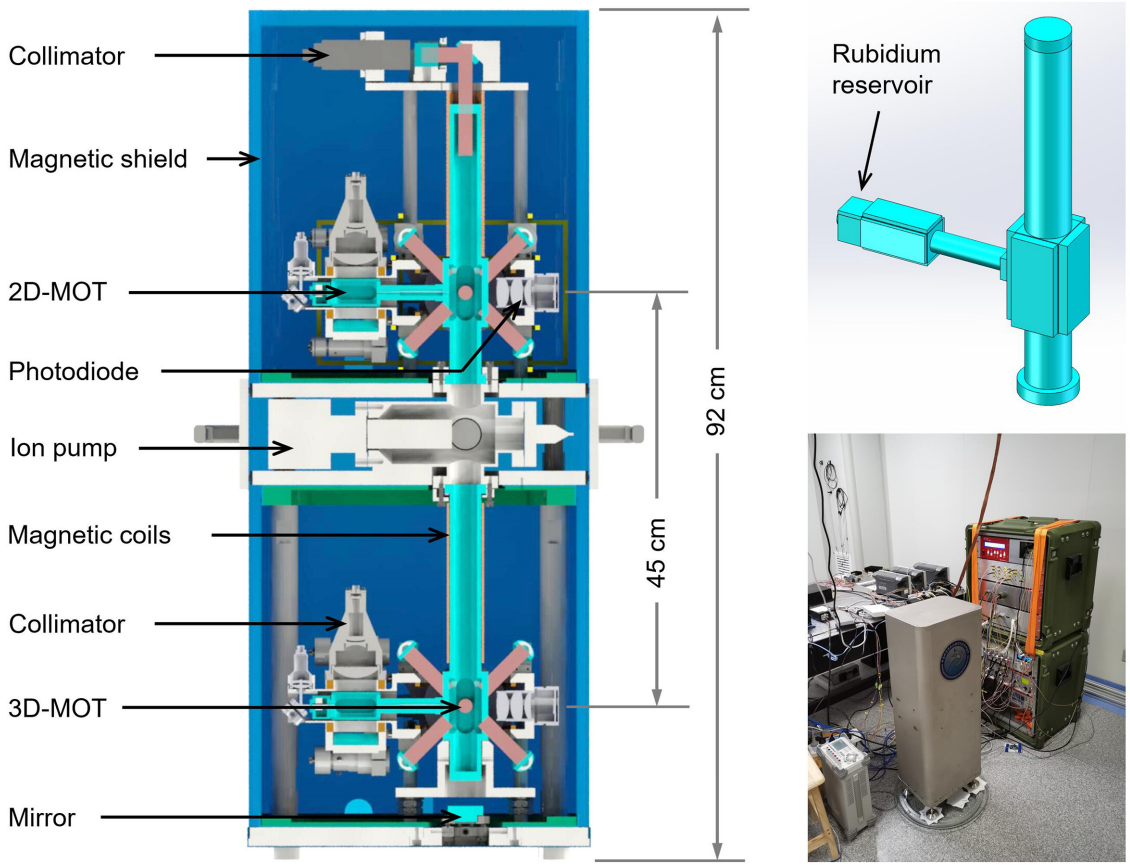

FIG. 1. The design drawing and a photograph of the atom-gravity gradiometer. The upper-right schematic is the vacuum chamber of the upper interferometer, made of silica. The gradiometer is composed of two vertically stacked AIs and each interferometer has its own two-dimensional (2D) and three-dimensional (3D) MOTs and atom fountain. The interference process is performed in the vacuum tubes above the two 3D MOTs by a common Raman laser beam penetrating the vacuum chamber from the top window and retroreflected by a mirror under the bottom window. The final detection process is performed in the region of the 3D MOTs when the atoms fall back after the coherent manipulations.

simplicity of the sensor head and laser system. To achieve a higher grade of common-mode noise rejection, the vacuum chambers of the two interferometers are connected at the propagation path of the Raman laser beam. The Raman laser delivered by a polarization-maintaining optical fiber is collimated into a 20-cm-diameter beam, which penetrates the vacuum chamber vertically from the top window and is retroreflected by a mirror under the bottom window. Since there is neither a window nor air between the two atom clouds, in comparison with the configuration based on two independent vacuum chambers [18], the phase error and noise induced by the beam-steering effect of the windows and the refractive-index variations of the air are eliminated. The axis of the gradiometer and the Raman laser beam are prealigned vertically by a liquid surface and the readings of an internal tilt meter (not strictly zero in most cases) are recorded. When this gradiometer is taken to a new place, we just adjust the supporting feet of the sensor head to make the tilt meter restore the readings; in this way, the instrument can be quickly leveled.

Although the physical structure of the sensor head is similar to our former generation [24], many improvements have been implemented. To squeeze the dimensions of the sensor head and increase the operating speed of the magnetic fields, with the exception of the connection unit of the vacuum pump, the vacuum chamber is entirely fabricated using JGS1 silica. Due to the active nature of alkali metals, the sample source is the most troublesome part for glass vacuum chambers. In previous glass chambers, the reservoir of alkali metal is still a piece of soft metal or is connected with a copper transmission pipe that cannot be removed [18,25]. Both solutions employ a series of metal screws and accessories, which makes the vacuum chamber complicated and malformed. In making our newly developed vacuum chamber, we freeze the rubidium samples to −200 K with liquid nitrogen to reduce their activity and then put the frozen samples directly into the silica reservoir and seal the chamber within a few minutes. By this method, two compact real-glass rubidium sample sources are realized, which enable the optical and

magnetic accessories for each 2D MOT to be integrated as one module and adjusted independently elsewhere. Then, the completed module is directly sheathed onto the 2D-MOT chamber from the terminal side, where the reservoir is located.

Due to the large aperture of the glass chamber and the elaborate design of interior space layout, with a 44.5-cm baseline and two 18-cm fountains, the height of the total sensor head including the two-layer magnetic shields is only 92 cm. To make full use of the vertical space in the sensor head, the final detection process is carried out in the region of the 3D MOTs when the atoms fall back down. Since the rubidium pressure in the 2D-MOT chambers is almost at its saturated vapor pressure and the distances between the 2D- and 3D-MOT chambers are as little as 7 cm, this design also leads to a detection-background issue. During the detection phase, many atoms from the 2D-MOT chambers with low axial velocities arrive in the detection regions and produce strong detection backgrounds, the amplitudes of which are even higher than that from the falling-back atoms. To solve this problem, before the atoms fall back down, we perform a horizontal blow-away operation in each region of the 3D MOT with a resonant laser beam along the axis of the 2D MOT. By means of this operation, most of the background atoms are removed and the corresponding signals are reduced by almost 90%.

A detailed description of the laser system can be found in Ref. [26]. All the units are integrated into a double-sided module with dimensions of 45 cm $\times$ 45 cm $\times$ 16 cm. Two diode lasers and two tapered amplifiers are employed in the system. The main laser is stabilized on the transition of $|5^2S_{1/2}, F = 3\rangle \rightarrow |5^2P_{3/2}, F' = 4\rangle$ and amplified by one of the amplifiers: it then serves for cooling, the fountain, the blow-away operation, detection, and Raman laser seeding. The other laser is stabilized on the transition $|5^2S_{1/2}, F = 2\rangle \rightarrow |5^2P_{3/2}, F' = 3\rangle$ and serves as a repumping laser. The Raman laser pair is sourced from the amplified main laser and generated by a 1.5 GHz AOM. The $(+1)$- and (-1)-order diffracted beams are recombined and injected into the other tapered amplifier. Therefore, a pair of Raman beams with a frequency difference equal to the $5^2S_{1/2}$ hyperfine splitting is obtained. In comparison with the method of phase locking and electro-optic modulation, this scheme avoids the risk of losing lock and complicated processing of the multisideband effects and thus results in higher robustness and measurement stability. Although there is no requirement for ultralow phase noise because our gradiometer is operating in differential mode, this Raman laser can work really well without phase stabilization even in a single interferometer (e.g., a gravimeter [26]) if the microwave driver is good enough. However, this configuration also leads to a minor issue with an imbalanced ac Stark shift and hence to a non-negligible measurement error. In this work, real-time feedback control of the intensity ratio is performed to eliminate this effect, which we describe in more detail in Sec. V. The laser and the control system are installed in two 12 U (1 U = 44.45 mm) 19-in. racks, each of which has dimensions of 62 cm $\times$ 65 cm $\times$ 67.5 cm. The power consumption of the total gradiometer is measured to be about 600 W.

Since there are no vibration isolation or compensation devices in the gravity gradiometer, each interferometer suffers from vibration noise. When operating in a quiet underground laboratory, both the interferometers could output clear fringes and serve as gravimeters. After we take the gradiometer to a noisy environment, the vibration noise completely disrupts the two individual signals and a fringe can no longer be read. However, as shown in Fig. 2, the differential ellipse shows very strong immunity and still maintains almost the same signal-to-noise ratio.

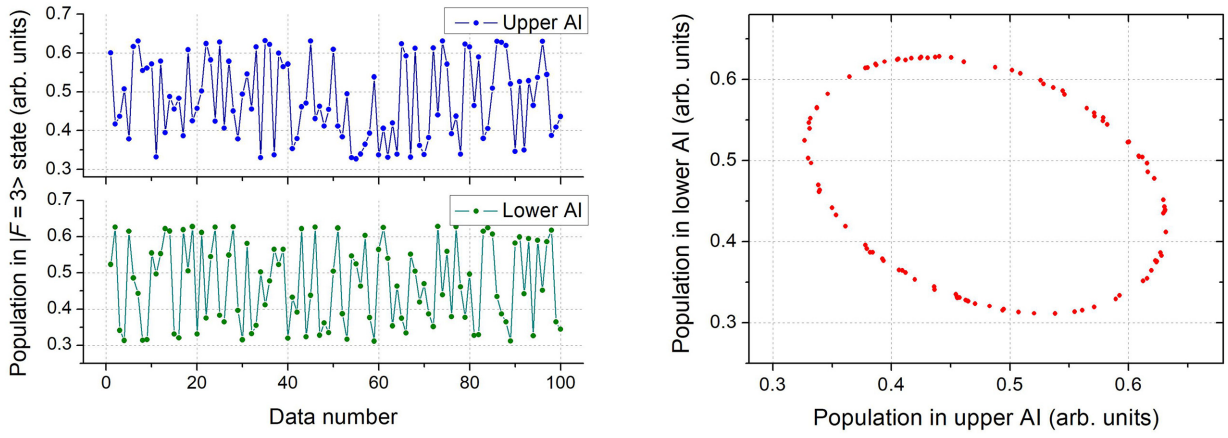

FIG. 2. The interferometer signals of the two AIs in the discrete and differential modes. The left and right graphs are from the same group of data with 100 measurements.

III. SENSITIVITY

For a quantum system with white noise, the measurement resolution R can be expressed as

$$R = S/\sqrt{\tau}, \tag{7}$$

where S is the sensitivity and τ is the measurement time. An improved measurement resolution R could be achieved by increasing the sensitivity S or extending the measurement time τ. Furthermore, for AIs based on discrete atom clouds, the sensitivity S is

$$S = N_s\sqrt{\delta t}, \tag{8}$$

where N_s is the single-shot noise and δt is the single measurement time. Therefore, both suppression of the single-shot noise N_s and reduction of the single measurement time δt help to improve the sensitivity.

Many works have reported methods to suppress the single-shot noise, such as active control of the critical parameters [27] and the utilization of normalized detection [28,29]. In this work, we investigate the dependence of the single-shot noise on the quantization magnetic field. As shown in Fig. 3, the ellipse phase noise has minimum values in the range 15–60 mA and increases significantly as the magnetic field increases due to the noise of the quadratic Zeeman shift. However, when the current decreases to 10 mA, the phase noise also increases drastically due to the loss of the quantization direction. According to this result, we choose a quantization magnetic current of 15 mA in the following experiments, which corresponds to a magnetic field of about 30 mG.

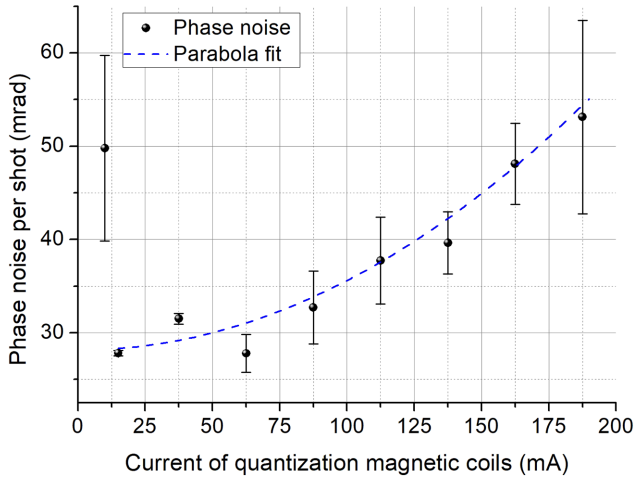

FIG. 3. The dependence of the single-shot noise on the current of the bias coils. Each point corresponds to three measurements of 40 min. According to the theoretical square relationship between the coil current and the phase noise induced by the quadratic Zeeman effect, the data points are fitted with a parabola function.

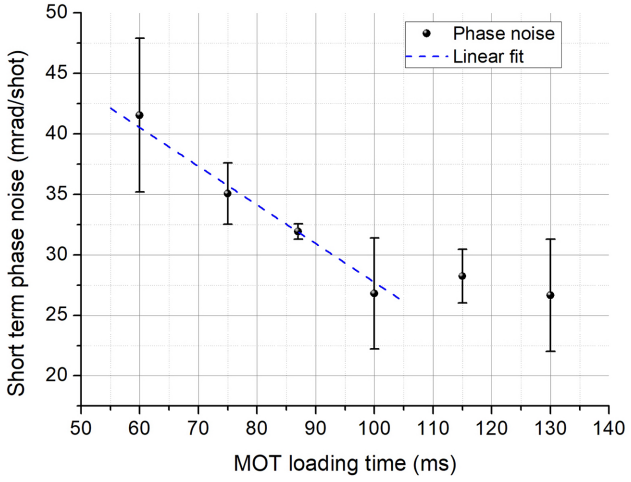

FIG. 4. The dependence of the single-shot noise on the MOT loading time.

From Eq. (8), we know that with a constant single-shot noise N_s, a higher data rate $1/\delta t$ also leads to a higher sensitivity S. Before the MOT is saturated, a longer loading time corresponds to a higher cold-atom number N and lower detection and quantum projection-noise limits. However, for a system with other technical noises that are higher than the two noise limits, a large atom number N does not correlate with reduced noise. On the contrary, as the loading time occupies a large part of the measurement time δt, the redundant loading time will in turn decrease the sensitivity S. Here, we investigate the relationship between the single-shot noise and the MOT loading time to find an optimal parameter that yields the highest sensitivity. The result is shown in Fig. 4: as the loading time increases, the single-shot noise decreases and reaches a nearly constant level. Theoretically, both phase noises caused by quantum projection and detection are inversely related to the atom number but the functional relationships are different. Given a detection noise with a constant amplitude, which comes from the detector and the detection laser, the corresponding phase noise will show a linear relationship with the signal amplitude, i.e., the atom number. In contrast, for the quantum projection noise, there is a well-known $1/\sqrt{N}$ relationship between the transferred phase noise and the atom number. Therefore, from Fig. 4, we know that the noise from detection is more dominant than that from quantum projection. Consequently, a loading time of 100 ms is chosen in the following experiments to achieve the highest sensitivity.

IV. LONG-TERM STABILITY

From Eq. (7), we know that in a white-noise system, the measurement resolution is inversely proportional to the square root of the measurement time τ. However, in AIs there is no technical noise that is completely white. Many

parameters, such as laser frequencies, laser intensities, and magnetic field strengths, vary with time and environmental factors, which induces long-term phase drifts in AIs. Here, we employ an algorithm relying on reversal of the Raman wave vector **k** to remove the k-polarity-independent drifts and improve the long-term stability of the gradiometer. We alternately measure the differential phase $\Delta\varphi$ with $+k$, the vector of which points downward, and $-k$, the vector of which points upward, and obtain

$$\Delta\varphi_{+k} = \Delta\varphi_{\text{ori\_indep}} + \Delta\varphi_{\text{ori\_dep}}, \tag{9a}$$

$$\Delta\varphi_{-k} = \Delta\varphi_{\text{ori\_indep}} - \Delta\varphi_{\text{ori\_dep}}. \tag{9b}$$

$\Delta\varphi_{\text{ori\_dep}}$ is the phase the polarity of which depends on the direction of the Raman wave vector **k**, which is usually induced by the gravity and rotation, while $\Delta\varphi_{\text{ori\_indep}}$ is the phase the polarity of which is independent of the direction of **k**, which is usually induced by the Zeeman shift, light shift, etc. Therefore, the phase $\Delta\varphi_{\text{ori\_dep}}$ including the effect of the gravity gradient can be extracted as

$$\Delta\varphi_{\text{ori\_dep}} = \frac{1}{2}(\Delta\varphi_{+k} - \Delta\varphi_{-k}). \tag{10}$$

We carry out a long-term interleaving measurement of $\Delta\varphi_{+k}$ and $\Delta\varphi_{-k}$ and the results are shown in Fig. 5. We can see that apparently synchronous phase drifts happen at $\Delta\varphi_{+k}$ and $\Delta\varphi_{-k}$, while the differential phase $(\Delta\varphi_{+k} - \Delta\varphi_{-k})/2$ shows high stability. The corresponding Allan deviations are shown in Fig. 6. In comparison with the measurement results of $\Delta\varphi_{+k}$ and $\Delta\varphi_{-k}$, the long-term stability of the differential phase is improved by an order of magnitude and reaches a level of 104 μrad after an averaging time of 17 000 s. For a gravity gradiometer with a baseline of $L = 44.5$ cm and an interrogation time of $T = 130$ ms, the corresponding resolution of the gravity gradient is 0.86 E. However, the Allan deviations of the differential phase do not decrease along a constant slope but deviate from the ideal trend from 1000 s to 14 000 s. This indicates residual factors with a specific period that are perturbing the measurement. Since this period is roughly in accordance with the temperature fluctuations in our laboratory, we plan to develop some temperature-control units (especially for the laser system) in the future.

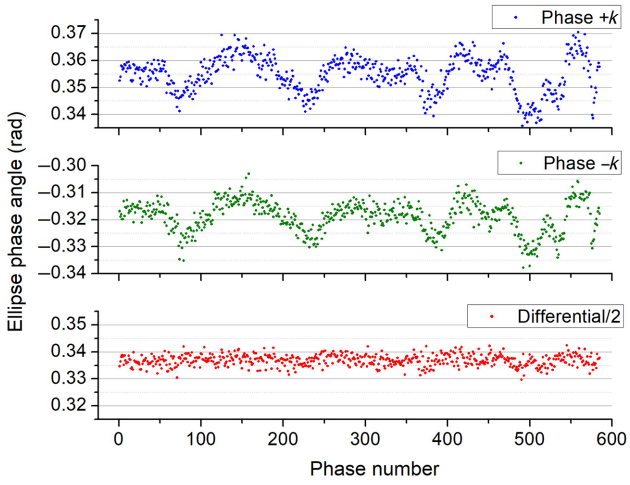

FIG. 5. Improvement of the long-term stability. The three sets of data (from top to bottom) are the phases $\Delta\varphi_{+k}$, $\Delta\varphi_{-k}$, and $(\Delta\varphi_{+k} - \Delta\varphi_{-k})/2$, respectively. Each data point of $\Delta\varphi_{+k}$ and $\Delta\varphi_{-k}$ is extracted from 40 measurements.

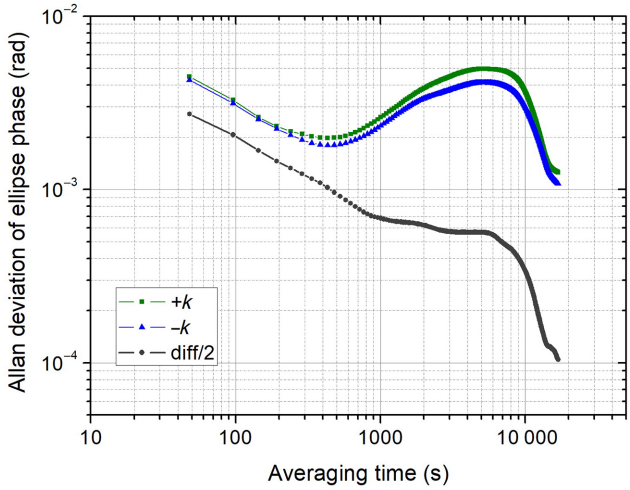

FIG. 6. Allan deviations for the ellipse phases in Fig. 4. Each data pair $\Delta\varphi_{+k}$ and $\Delta\varphi_{-k}$ is extracted from 80 measurements and takes 48 s.

V. MEASUREMENT ERRORS

For an absolute-gravity gradiometer, the accuracy is another important technical index in addition to the sensitivity and the long-term stability. Although gradiometers have error sources similar to those of gravimeters, the role played by each source is different. Due to the mechanism of common-mode rejection, many important errors in atom gravimeters are negligible in gravity gradiometers. Most of them are related to Raman laser phases, such as those caused by laser path variation [9] and synchronous vibration [4,9]. In addition, unlike the gravimeters with targets to resolve ng signals from a background of $1g$, for gradiometers to distinguish 1 E from 10^3 E, the error caused by the inaccuracy of the laser frequency also does not need to be considered.

In contrast, some insignificant errors in atom gravimeters, such as that induced by light shift, play more significant roles in our gradiometer. Specifically, the differential ac Stark shift at each Raman laser pulse is given by

$$\delta^{\text{ac}} = \Omega_a^{\text{ac}} - \Omega_b^{\text{ac}} = \sum_{m,i}\left(\frac{|\Omega_{a,i,m}|^2}{4\Delta_{a,i,m}} + \frac{|\Omega_{b,i,m}|^2}{4\Delta_{b,i,m}}\right), \tag{11}$$

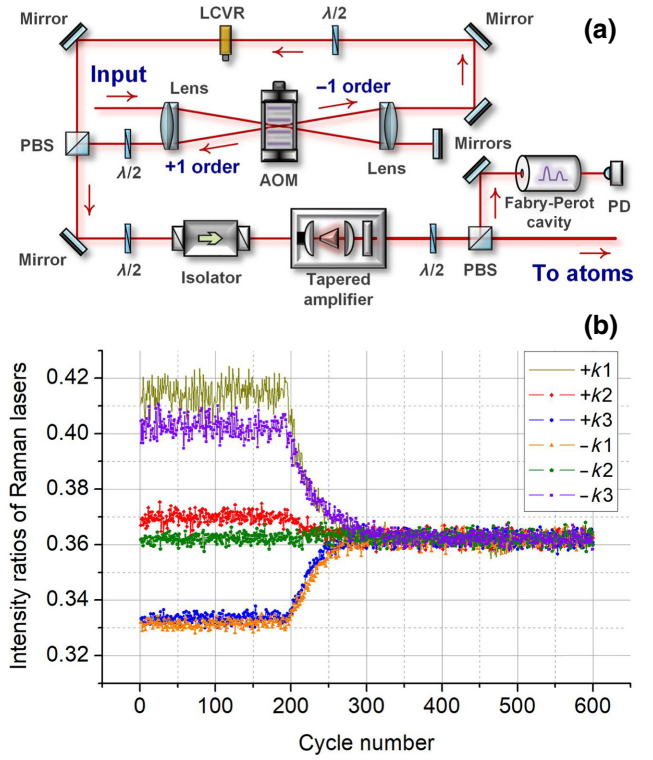

FIG. 7. (a) A schematic of the Raman laser (PBS: polarizing beam splitter, LCVR: liquid-crystal variable retarder, PD: photo detector). (b) The effect of feedback control of the laser intensity ratios. The (+1)- and (−1)-order diffracted light beams of the AOM are combined via a PBS and amplified simultaneously by a tapered amplifier. A LCVR is utilized to adjust the injecting intensity ratio of the two Raman beams. $+ki$ and $-ki$ denote the ith pulse in $+k$ and $-k$ measurements respectively.

where Ω is the one-photon Rabi frequency, Δ is the detuning, a, b, and i, respectively, denote the two ground states and the excited state in the stimulated Raman transition, and m is the index of the light field. Usually, an optimal intensity ratio of the Raman laser components is set to cancel out the ac Stark shift δ^{ac} to zero. However, in our Raman laser scheme [shown in Fig. 7(a)], both the diffraction efficiency of the AOM and the amplification efficiency of the tapered amplifier (TA) vary with the modulation frequency. Therefore, the intensity ratio changes from pulse to pulse when the frequency is chirping to compensate the gravity-induced Doppler shift. During a cycle consisting of a $+k$ and a $-k$ measurement, a total of six modulation frequencies are employed, which results in six intensity ratios.

The corresponding phase shift in each $+k$ and $-k$ measurement is

$$\Delta\varphi^{\mathrm{ac}} = 2(\delta_1^{\mathrm{ac}} - \delta_3^{\mathrm{ac}})\tau, \tag{12}$$

where δ_1^{ac} and δ_3^{ac} are the ac Stark shifts at the first and the last Raman pulses, respectively. Since all the intensity ratios are probably different from each other, this phase shift cannot be canceled within one AI. In addition, the projections of the two atom trajectories on the Gaussian beam cross section cannot be exactly overlapped, which makes the light shifts different in the two AIs. Therefore, this phase shift also cannot be completely rejected by differential measurement between AIs.

To solve this problem, we program real-time feedback control of the intensity ratio between the Raman laser components. A Fabry-Perot cavity is employed to read the intensity ratio and a liquid-crystal variable retarder (LCVR) is used to perform the adjustment. Since the input beam is first diffracted to the −1 order, which makes the original intensity of the (−1)-order beam 1.5 times that of the +1 order, a LCVR in the path of the (−1)-order beam could achieve the maximum adjustment range of the intensity ratio. The effect of the control loop is shown in Fig. 7(b). In free-running mode, the intensity ratios are distributed from 0.33 to 0.42. When the feedback is turned on, within 100 cycles, all the ratios are drawn to the set value of 0.362, which is the optimal intensity ratio determined by earlier experiment. With respect to the ellipse phase, an offset of $+11.0 \pm 0.8$ mrad is observed after the feedback control is turned on, which corresponds to a gravity gradient of $+91 \pm 6$ E.

The error caused by the Zeeman effect has already been studied in Ref. [20]. In this work, as described in Sec. IV, we perform interleaving measurements by reversing the direction of the Raman wave vector; thus this effect should be eliminated in principle. However, when we scan the quantization magnetic fields, as shown in Figs. 8 and 9, although the phase shifts are significantly attenuated by the algorithm, there remains an obvious relationship between the differential phase $(\Delta\varphi_{+k} - \Delta\varphi_{-k})/2$ and the magnetic

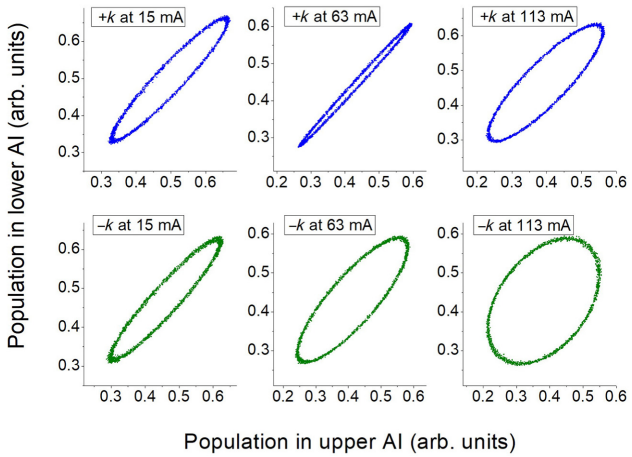

FIG. 8. Ellipses in different magnetic fields. Since ellipse fitting can only give results within $[0, \pi]$, we need to combine theoretical predictions to distinguish the sign of the phase; e.g., from the evolution trend of the $+k$ ellipse shape, we can conclude that the phase has undergone a polarity reversal.

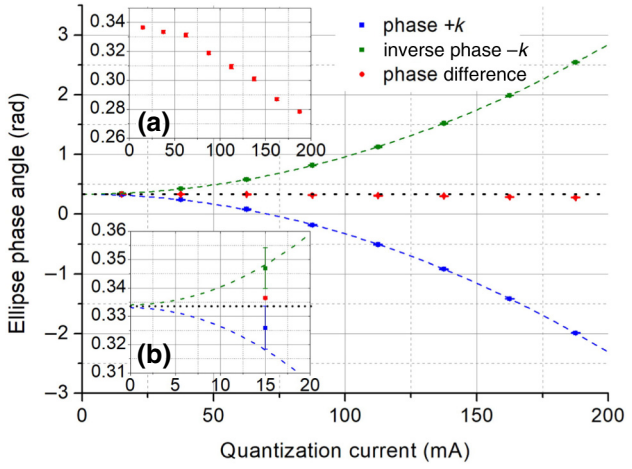

FIG. 9. The dependence of the ellipse phase on the quantization magnetic field. The magnetic fields are scanned three times and within each scan, eight measurements, each of duration 40 min, are taken. The dashed lines are parabola-fitted results for $+k$ and $-k$ modes, respectively. Insets (a) and (b) are the corresponding enlarged parts of the main curve.

fields [shown in Fig. 9(a)]. This is probably caused by the difference between the atom trajectories in the two measurement modes. Since the atoms obtain a recoil velocity of approximately 12 mm/s from a Raman laser pulse, there should be an approximately 3-mm maximum offset of the average position between the $+k$ and $-k$ interferometers. That induces different experiences for atoms in nonuniform magnetic fields. Finally, we derive the corrected phase value by extrapolating the two parabola-fitted curves to zero field. As shown in the inset of Fig. 9(b), the results from the $+k$ and $-k$ interferometers are highly consistent within 1 mrad. Therefore, we evaluate a Zeeman correction phase of -3.0 ± 1.0 mrad, which corresponds to a gravity-gradient offset of -25 ± 8 E.

The sensitivity to rotation is sometimes useful for AIs, which can be employed to make gyroscopes. However, in gravimeters, this sensitivity leads to one of the most significant measurement errors due to the Coriolis effect. Specifically, the rotation-induced phase shift is given by

$$\Delta\varphi_{\text{Coriolis}} = \mathbf{k}_{\text{eff}} \cdot (\Omega_{\text{Earth}} \times \mathbf{v})T^2, \tag{13}$$

where Ω_{Earth} is the Earth's rotational angular velocity and $\mathbf{v}$ is the average velocity of atoms. In our gradiometer, since the wave vector $\mathbf{k}_{\text{eff}}$ is vertical and the Earth rotates along the axis pointing north, this phase is sensitive to the velocity component along the east-west direction. Many imperfect experimental conditions, such as misalignment and the power imbalance of the cooling laser beams, lead to a nonzero average horizontal velocity of atoms. In juggling-type atom-gravity gradiometers, where the two atom clouds are launched by a same group of lasers and tend to acquire similar horizontal velocities, this Coriolis phase shift can be significantly canceled. However, in our gravity gradiometer, the two atom clouds come from different MOTs and are launched by different groups of lasers. This puts the two atom clouds at great risk of having different horizontal velocities. Therefore, we must take this effect as seriously as we do in the gravimeters. Usually, the method of synchronously rotating the Raman laser mirror opposite to the direction of the Earth's rotation is used to eliminate this phase shift. However, this is not necessary for a mobile instrument. Here, we employ a method of interleaving the orientation of the sensor head to evaluate this Coriolis error.

The ellipse phase shifts for an atom-gravity gradiometer with opposite horizontal orientations, 0° and 180°, can be written as

$$\begin{aligned}\Delta\varphi_0 &= \Delta\varphi_{gg} + \Delta\varphi_{\text{Coriolis\_0}} \\ &= \mathbf{k}_{\text{eff}} \cdot \Delta\mathbf{g}T^2 + \mathbf{k}_{\text{eff}} \cdot (\Omega_{\text{Earth}} \times \Delta\mathbf{v}_h)T^2, \qquad (14a)\\ \Delta\varphi_{180} &= \Delta\varphi_{gg} + \Delta\varphi_{\text{Coriolis\_180}} \\ &= \mathbf{k}_{\text{eff}} \cdot \Delta\mathbf{g}T^2 - \mathbf{k}_{\text{eff}} \cdot (\Omega_{\text{Earth}} \times \Delta\mathbf{v}_h)T^2. \qquad (14b)\end{aligned}$$

When the orientation is reversed, the phase shift induced by the gravity gradient $\Delta\varphi_{gg}$ remains the same, while that induced by the Earth's rotation is reversed in sign. Therefore, the Coriolis phase shift can be evaluated by

$$\Delta\varphi_{\text{Coriolis}} = (\Delta\varphi_0 - \Delta\varphi_{180})/2 \tag{15}$$

and the corrected measurement phase is

$$\Delta\varphi_{gg} = (\Delta\varphi_0 + \Delta\varphi_{180})/2. \tag{16}$$

The experimental results are shown in Fig. 10, where each measurement takes 30 min. We can see that the

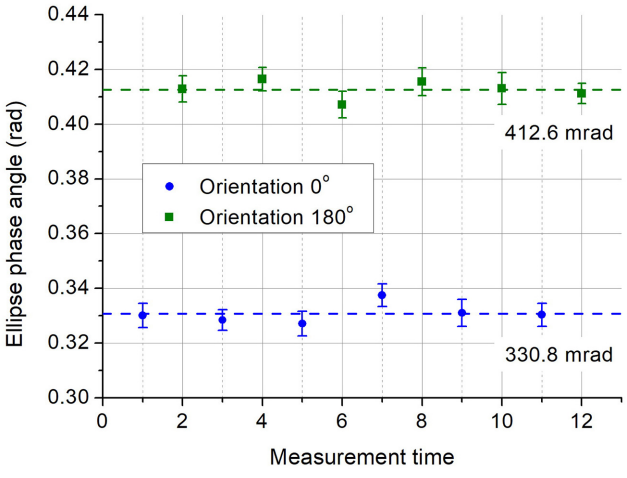

FIG. 10. The dependence of the ellipse phase angle on the horizontal orientation of the sensor head. Each measurement takes 30 min.

phase difference in the two situations is stable over 12 interleaved measurements. Finally, from that we derive the corrected phase shift, $\Delta\varphi_{gg} = 371.7 \pm 4.9$ mrad, and the phase offset induced by the Coriolis effect, $\Delta\varphi_{\text{Coriolis}} = -40.9 \pm 4.9$ mrad, which corresponds to a gravity gradient of 338 ± 40 E.

The self-attraction effect is another important error source in both atom gravimeters and gravity gradiometers [30,31]. Here, we calculate the self-attraction field by the finite-element method and the induced phase shifts are computed through the perturbation path integral treatment. The self-attraction fields caused by different parts of the sensor head are shown in Fig. 11. In the previous apparatus, most of the mass is distributed on one side of the interference region and produces a relatively smooth curve. However, in our gravity gradiometer with two discrete sets of 2D and 3D MOTs, interference regions, and, especially, a common pump unit in the middle of the two interferometers, the mass distribution is much more scrambled and leads to fluctuating curves. Among those attractive sources, though the magnetic shields account for more than one third of the total mass, they contribute little to the total attractive field for their symmetrical distributions around the interferometers. On the contrary, the frames and coils play the most important roles due to their close proximity to the interference regions. The induced phase shift in each interferometer is given by

$$\begin{aligned}\Delta\varphi &= \frac{1}{\hbar}\int_0^{2T}(L^I_{\text{pert}}[z(t),\dot{z}(t)] - L^{II}_{\text{pert}}[z(t),\dot{z}(t)])dt \\ &= -k_{\text{eff}}\left(\int_0^T t a_{\text{pert}}(t)dt + \int_T^{2T}(2T-t)a_{\text{pert}}(t)dt\right),\end{aligned} \tag{17}$$

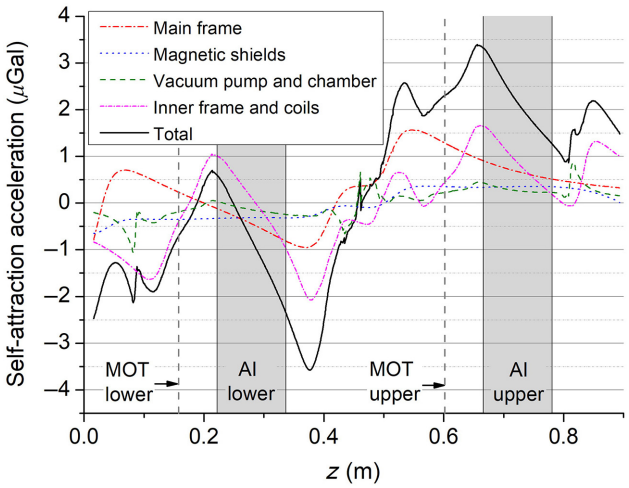

FIG. 11. The self-attraction accelerations along the vertical direction caused by different parts of the sensor head. The vertical dashed lines indicate the positions of the two MOTs and the gray shading indicates the interference regions. The position $z = 0$ corresponds to the bottom of the sensor head.

TABLE I. The systematic error budget.

Systematic effect	Correction (E)	Uncertainty (E)
Laser frequency	0	< 0.1
Vibration	0	< 0.1
Vertical alignment	0	< 0.1
Baseline	0	4
Raman wave fronts	0	33
Ellipse fitting	−14	5
ac Stark shift	+91	6
Magnetic effect	−25	8
Coriolis effect	+338	40
Self-attraction	+77	5
Total	+467	53

where the L^i_{pert} are the perturbed Lagrangians along the interferometer path I and II and $a_{\text{pert}}(t)$ is the perturbed acceleration along the z axis (vertical direction). Then, we obtain the offset of the measured g induced by the self-attraction

$$\delta g = \frac{1}{T^2}\left(\int_0^T t a_{\text{pert}}(t)dt + \int_T^{2T}(2T-t)a_{\text{pert}}(t)dt\right). \tag{18}$$

Combining with atom trajectories, we obtain the offset of the measured differential gravity $\delta g = \delta g_1 - \delta g_2 = 3.43\ \mu$ Gal, which corresponds to a gravity gradient of −77 E with a baseline of 44.5 cm. Although the trajectory deflections caused by the photon recoil momenta are also considered in our calculation, the difference between the $+k$ and $-k$ measurements is found to be only 0.3 E. In addition, taking into account the neglected small components, the nonuniform density distribution of commercial devices, nonzero atom-cloud sizes, etc., we estimate that the uncertainty of this offset is about 5 E.

The systematic errors and the uncertainties are summarized in Table I, where the Coriolis effect leads to the dominant offset and uncertainty. In principle, the error caused by Raman wave-front distortion could be common-mode rejected supposing that the two atom clouds are perfectly overlapped on the beam cross section and expand synchronously. However, that ideal situation rarely occurs: we therefore estimate this uncertainty to be 33 E under the condition that the mirror and the vacuum window distort the wave front to $\lambda/5$ and the two atom clouds separate horizontally by 1 mm. From the above budget, we measure the local gravity gradient and obtain the corrected result as 3114 ± 53 E, which agrees with the mean free-air value of 3090 E [32].

VI. CONCLUSION AND DISCUSSION

We develop a compact high-resolution absolute-gravity gradiometer based on dual ^{85}Rb LPAIs for the measurement of the vertical component of the gravity gradient.

Two all-glass vacuum chambers are designed and fabricated, which suppress the volume of the sensor head down to 95 l. The weight of the sensor head is only 66.4 kg and it can easily be handled by two people. In addition to the optimization of many experimental parameters for sensitivity improvement, the method of wave-vector reversal is also implemented, which demonstrates the remarkable power of long-term drift suppression. Finally, a measurement resolution as low as 0.86 E is achieved after an integration of 17 000 s. Therefore, this sub-E atom-gravity gradiometer has one of the highest levels of compactness to date. The compactness of the sensor head should be very convenient when taking it onto forms of transportation where space is at a premium and demonstrates significant advantage in matching with inertial stabilized platforms, the precision of which is sensitive to the dimension of the load. In addition, the systematic errors are carefully evaluated. A special error, ac-Stark-shift imbalance, caused by the Raman laser scheme based on a chirping AOM, is found and eliminated. Making use of this gravity gradiometer, we measure the local absolute-gravity gradient and obtain a result of 3114 ± 53 E, which agrees well with the reference mean free-air value.

The performance of the gravity gradiometer can be further improved in the future. The weight of the sensor head can easily be decreased to less than 50 kg by optimization of the supporting structure. The detection noise is probably the limit to the short-term sensitivity: it can be decreased by active control of the intensity of the detection laser and the utilization of detectors with lower noise. The simultaneous detection of two atomic states [28] and the method of phase-shear readout [33,34], which make the detection insensitive to fluctuations of the laser frequency and intensity, are also schemes that are very much worth trying. The residual long-term drift is mainly caused by the thermal effect of the optical fibers: therefore, temperature control of critical components will be helpful to improve the long-term stability. With respect to the accuracy, the Coriolis error could be evaluated more accurately by using a precision rotation platform and the uncertainty caused by the effect of wave-front distortion could be reduced through the extrapolation experiment of beam-size modulation [35].

ACKNOWLEDGMENTS

We acknowledge the financial support from the National Key Research and Development Program of China under Grant No. 2016YFA0302002, the National Natural Science Foundation of China under Grants No. 91536221 and No. 91736311, and the Strategic Priority Research Program of the Chinese Academy of Sciences under Grant No. XDB21010100.

[1] M. Kasevich and S. Chu, Atomic Interferometry using Stimulated Raman Transitions, Phys. Rev. Lett. **67**, 181 (1991).

[2] Z. K. Hu, B. L. Sun, X. C. Duan, M. K. Zhou, L. L. Chen, S. Zhan, Q. Z. Zhang, and J. Luo, Demonstration of an ultrahigh-sensitivity atom-interferometry absolute gravimeter, Phys. Rev. A **88**, 043610 (2013).

[3] T. Farah, P. Gillot, B. Cheng, A. Landragin, S. Merlet, and F. P. Dos Santos, Effective velocity distribution in an atom gravimeter: Effect of the convolution with the response of the detection, Phys. Rev. A **90**, 023606 (2014).

[4] C. Freier, M. Hauth, V. Schkolnik, B. Leykauf, M. Schilling, H. Wziontek, H. G. Scherneck, J. Muller, and A. Peters, Mobile quantum gravity sensor with unprecedented stability, J. Phys. Conf. Ser. **723**, 012050 (2016).

[5] V. Menoret, P. Vermeulen, N. Le Moigne, S. Bonvalot, P. Bouyer, A. Landragin, and B. Desruelle, Gravity measurements below 10^{-9} g with a transportable absolute quantum gravimeter, Sci. Rep. **8**, 12300 (2018).

[6] J. Fang, J. G. Hu, X. Chen, H. R. Zhu, L. Zhou, J. Q. Zhong, J. Wang, and M. S. Zhan, Realization of a compact one-seed laser system for atom interferometer-based gravimeters, Opt. Express **26**, 1586 (2018).

[7] Z. J. Fu, B. Wu, B. Cheng, Y. Zhou, K. X. Weng, D. Zhu, Z. Y. Wang, and Q. Lin, A new type of compact gravimeter for long-term absolute gravity monitoring, Metrologia **56**, 025001 (2019).

[8] S. K. Wang, Y. Zhao, W. Zhuang, T. C. Li, S. Q. Wu, J. Y. Feng, and C. J. Li, Shift evaluation of the atomic gravimeter NIM-AGRb-1 and its comparison with FG5X, Metrologia **55**, 360 (2018).

[9] P. W. Huang, B. Tang, X. Chen, J. Q. Zhong, Z. Y. Xiong, L. Zhou, J. Wang, and M. S. Zhan, Accuracy and stability evaluation of the Rb-85 atom gravimeter WAG-H5-1 at the 2017 International Comparison of Absolute Gravimeters, Metrologia **56**, 045012 (2019).

[10] Z. J. Fu, Q. Y. Wang, Z. Y. Wang, B. Wu, B. Cheng, and Q. Lin, Participation in the absolute gravity comparison with a compact cold atom gravimeter, Chin. Opt. Lett. **17**, 011204 (2019).

[11] Y. Bidel, N. Zahzam, C. Blanchard, A. Bonnin, M. Cadoret, A. Bresson, D. Rouxel, and M. F. Lequentrec-Lalancette, Absolute marine gravimetry with matter-wave interferometry, Nat. Commun. **9**, 627 (2018).

[12] Y. Bidel, N. Zahzam, A. Bresson, C. Blanchard, M. Cadoret, A. V. Olesen, and R. Forsberg, Absolute airborne gravimetry with a cold atom sensor, J. Geodesy **94**, 20 (2020).

[13] M. J. Snadden, J. M. McGuirk, P. Bouyer, K. G. Haritos, and M. A. Kasevich, Measurement of the Earth's Gravity Gradient with an Atom Interferometer-Based Gravity Gradiometer, Phys. Rev. Lett. **81**, 971 (1998).

[14] J. M. McGuirk, G. T. Foster, J. B. Fixler, M. J. Snadden, and M. A. Kasevich, Sensitive absolute-gravity gradiometry using atom interferometry, Phys. Rev. A **65**, 033608 (2002).

[15] J. B. Fixler, G. T. Foster, J. M. McGuirk, and M. A. Kasevich, Atom interferometer measurement of the Newtonian constant of gravity, Science **315**, 74 (2007).

[16] F. Sorrentino, Y. H. Lien, G. Rosi, L. Cacciapuoti, M. Prevedelli, and G. M. Tino, Sensitive gravity-gradiometry

with atom interferometry: Progress towards an improved determination of the gravitational constant, New J. Phys. **12**, 095009 (2010).

[17] G. Rosi, F. Sorrentino, L. Cacciapuoti, M. Prevedelli, and G. M. Tino, Precision measurement of the Newtonian gravitational constant using cold atoms, Nature **510**, 518 (2014).

[18] G. W. Biedermann, X. Wu, L. Deslauriers, S. Roy, C. Mahadeswaraswamy, and M. A. Kasevich, Testing gravity with cold-atom interferometers, Phys. Rev. A **91**, 033629 (2015).

[19] D. K. Mao, X. B. Deng, H. Q. Luo, Y. Y. Xu, M. K. Zhou, X. C. Duan, and Z. K. Hu, A dual-magneto-optical-trap atom gravity gradiometer for determining the Newtonian gravitational constant, Rev. Sci. Instrum. **92**, 053202 (2021).

[20] F. Sorrentino, A. Bertoldi, Q. Bodart, L. Cacciapuoti, M. de Angelis, Y. H. Lien, M. Prevedelli, G. Rosi, and G. M. Tino, Simultaneous measurement of gravity acceleration and gravity gradient with an atom interferometer, Appl. Phys. Lett. **101**, 114106 (2012).

[21] C. Janvier, V. Menoret, B. Descruelle, S. Merlet, A. Landragin, and F. P. Dos Santos, Compact differential gravimeter at the quantum projection-noise limit, Phys. Rev. A **105**, 022801 (2022).

[22] B. Stray *et al.*, Quantum sensing for gravity cartography, Nature **602**, 590 (2022).

[23] G. T. Foster, J. B. Fixler, J. M. McGuirk, and M. A. Kasevich, Method of phase extraction between coupled atom interferometers using ellipse-specific fitting, Opt. Lett. **27**, 951 (2002).

[24] Y. P. Wang, J. Q. Zhong, H. W. Song, L. Zhu, Y. M. Li, X. Chen, R. B. Li, J. Wang, and M. S. Zhan, Location-dependent Raman transition in gravity-gradient measurements using dual atom interferometers, Phys. Rev. A **95**, 053612 (2017).

[25] K. X. Weng, B. Wu, J. H. Lin, Y. Zhou, B. Cheng, and Q. Lin, Compact magneto-optical trap with a quartz vacuum chamber for miniature gravimeters, J. Opt. Soc. Am. B **37**, 1637 (2020).

[26] X. W. Zhang, J. Q. Zhong, B. A. Tang, X. Chen, L. Zhu, P. W. Huang, J. Wang, and M. S. Zhan, Compact portable laser system for mobile cold atom gravimeters, Appl. Opt. **57**, 6545 (2018).

[27] F. Sorrentino, Q. Bodart, L. Cacciapuoti, Y. H. Lien, M. Prevedelli, G. Rosi, L. Salvi, and G. M. Tino, Sensitivity limits of a Raman atom interferometer as a gravity gradiometer, Phys. Rev. A **89**, 023607 (2014).

[28] G. W. Biedermann, X. Wu, L. Deslauriers, K. Takase, and M. A. Kasevich, Low-noise simultaneous fluorescence detection of two atomic states, Opt. Lett. **34**, 347 (2009).

[29] E. Rocco, R. N. Palmer, T. Valenzuela, V. Boyer, A. Freise, and K. Bongs, Fluorescence detection at the atom shot noise limit for atom interferometry, New J. Phys. **16**, 093046 (2014).

[30] G. D'Agostino, S. Merlet, A. Landragin, and F. P. Dos Santos, Perturbations of the local gravity field due to mass distribution on precise measuring instruments: A numerical method applied to a cold atom gravimeter, Metrologia **48**, 299 (2011).

[31] H. Zhang, D. K. Mao, Q. Luo, Z. K. Hu, L. L. Chen, and M. K. Zhou, The self-attraction effect in an atom gravity gradiometer, Metrologia **57**, 045011 (2020).

[32] W. Torge, *Gravimetry* (de Gruyter, Berlin, 1989).

[33] A. Sugarbaker, S. M. Dickerson, J. M. Hogan, D. M. S. Johnson, and M. A. Kasevich, Enhanced Atom Interferometer Readout through the Application of Phase Shear, Phys. Rev. Lett. **111**, 113002 (2013).

[34] J. M. Kwolek and A. T. Black, Continuous Sub-Doppler-Cooled Atomic Beam Interferometer for Inertial Sensing, Phys. Rev. Appl. **17**, 024061 (2022).

[35] M. K. Zhou, Q. Luo, L. L. Chen, X. C. Duan, and Z. K. Hu, Observing the effect of wave-front aberrations in an atom interferometer by modulating the diameter of Raman beams, Phys. Rev. A **93**, 043610 (2016).